4.1. Introduction

Metal-Organic Frameworks (MOFs) are a new class of crystalline materials consisting of 2D/3D networks formed by the nucleation of the metal centers and bridging organic ligand(s)[1–3]. Recently, MOFs have been widely utilized in the field of energy conversion, energy storage, catalysis, gas sorption, gas separation, sensor, and direct electrochemical applications.[4–8] Moreover, MOFs have been explored in the tribology due to their attractive properties like large surface area, tunable porosity, and excellent thermal and chemical stability.[9] Zeolitic imidazolate framework (ZIF- a sub-class of MOF) has been recently employed in tribology. Various ZIF such as ZIF-7, ZIF-9, ZIF-11, ZIF-12 have been reported with excellent performance in the triboelectric nanogenerator. ZIF-8 and ZIF-67 have also been employed as additives in lubricants to reduce friction.[10,11] Similarly, the self-lubricating properties of the nanocomposites of mesoporous Cu-BTC-MOFs have been investigated.[12]

In addition, a series of 2D materials such as graphitic carbon nitride, metal chalcogenides, layered metal hydroxides, graphene, etc., attain immense attention in tribology due to their high mechanical strength and flexibility.[13,14] 2D materials have been employed as the additive to increase the lubricant properties, and it has been observed that the morphology of the nanomaterials plays a significant role in the tribology. For example, ultrathin Zn-BDC was reported recently exhibiting excellent lubricant property.[15] Even recent tribological studies in our lab with a wide variety of additives heterocyclic organic compounds,[16–18] nanoparticles, and their composites,[19,20] nanohybrids of carbon spheres and nanoparticles,[21,22] graphene-based nanohybrids,[23–25] nano lamellar molybdenum

disulfide,[26] and so on have revealed that nano lamellar structures showed excellent performance.

These studies have inspired us to develop ultrathin Mn-MOF nanosheets [Mn-MOF (U)] and compare the tribo activity with the bulk materials [Mn-MOF (B)]. For this purpose, we have developed a unique method for the synthesis of ultrathin Mn-MOF nanosheets [Mn-MOF (U)] by coordinatively saturating the axial position of the metal ions with strong sigma donating ligand (triethylamine) along with the bridging ligand 1,4-benzene dicarboxylic acid (BDC). Triethylamine occupies the axial position of the metal centers and seizes the 3D growth of the MOF to form ultrathin nanosheets (Scheme 1).

It should be mentioned here that the previous synthesis of ultrathin MOF was reported either by the hydrothermal method or by liquid-phase exfoliation of the bulk MOF.[27–29] Ultrathin MOF synthesized by the hydrothermal method requires high temperature and pressure and the quality of the nanosheets is not satisfactory.[27] On the other hand, the liquid phase exfoliation of the bulk MOF results in the fragmentation of the nanosheets.[28,29] As a result, ultrathin MOF nanosheets synthesized by the exfoliation method have small size and poor quality. The yield of the MOF nanosheets is also a matter of concern as a large amount of sample is required in tribology. The present method allows us to produce ultrathin MOF nanosheets in gram scale with an average thickness of 9 nm. Tribological results based on several parameters such as mean wear scar diameter (MWD), the average coefficient of friction (COF), and load-carrying ability revealed ameliorated performance of Mn-MOF (U) compared to Mn-MOF (B).

4.2. Experimental section

4.2.1. Synthesis of additives

4.2.1.1 Synthesis of ultrathin Mn-MOF nanosheets/Mn-MOF (U)

Dimethylformamide (32 mL), ethanol (2 mL), and water (2 mL) were mixed in a 100 mL round bottom flask to get a homogeneous solution. 1,4-benzene dicarboxylic acid (BDC, 0.75 mmol) was dissolved in it, followed by the addition of $Mn(OAc)_2.4H_2O$ (0.75 mmol). Immediately, TEA (triethylamine, 0.8 mL) was added to the above mixture (at a time) and stirred for 5 min to obtain a colloidal suspension. The colloidal suspension was continuously sonicated for 4 h at room temperature under a nitrogen atmosphere. Finally, the product was collected by centrifugation at 8000 RPM, washed with ethanol for 5 times, and dried at room temperature in a vacuum.

4.2.1.2. Synthesis of bulk Mn-MOF/Mn-MOF (B)

Bulk Mn-MOF was synthesized by a similar method to Mn-MOF (U) without adding TEA in the solution of $Mn(OAc)_2.4H_2O$ and 1,4-benzene dicarboxylic acid.[30]

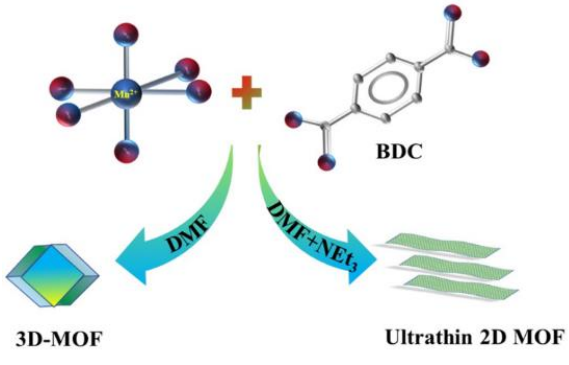

Scheme 4.1. Schematic illustration for the synthesis of ultrathin Mn-MOF (U) nanosheets by saturating the coordination sites of the metal ions with triethylamine in the presence of bridging ligand 1,4-benzene dicarboxylic acid

4.2.2. Sample Preparation

Test samples of different concentrations in the PO, 0.00, 0.10, 0.15, 0.20 and 0.25% w/v were prepared via 1 h sonication at room temperature. The tribological tests were performed at an optimized concentration, i.e., 0.15% w/v in base oil.

4.3. Results and discussion

4.3.1. Synthesis and Characterization of the MOFs

3D Mn-MOF was synthesized by the reaction of Mn^{2+} salt with the bridging ligand BDC. A huge change in the morphology and dimension of the MOF particles was observed when triethylamine was added to the solution of Mn^{2+} and BDC. Triethylamine seizes the 3D growth of the MOF by occupying the axial positions of the metal ions in an octahedral arrangement. The Powder X-ray diffraction (P-XRD) pattern confirms the crystal structure of Mn-MOF (U), and the pattern is exactly matching with the previous report (Figure 4.1a).[30] Mn-MOF (U) crystallized in a monoclinic system ($a \neq b \neq c$, $\alpha = \gamma = 90^0 \neq \beta$), having space group C2/c.[30] The peaks were detected at 2 theta values of 9.58°, 14.37°, 18.30° and indexed for the planes (200), (100), and (400), respectively. Mn-MOF (U) has the formula $[Mn_4(BDC)_4(NEt_3)_8]$, where the Mn ions are bonded with four oxygen atoms of the carboxylate groups of BDC, whereas two axial positions of the octahedra are occupied by TEA. As the Z-direction growth is seized by the addition of TEA, the MOF crystallizes as 2D material. The monolayers of Mn-MOF (U) were extracted by the top-down approach during the synthesis, i.e., by weakening the van der Waals forces between the layers with ultrasonication. Similarly, the PXRD of Mn-MOF (B) showed a similar pattern to Mn-MOF (U), while a slight shift of the peak positions

was observed (Figure 4.2a). The shift corresponding to the plane (200) was calculated to be 0.004 nm.

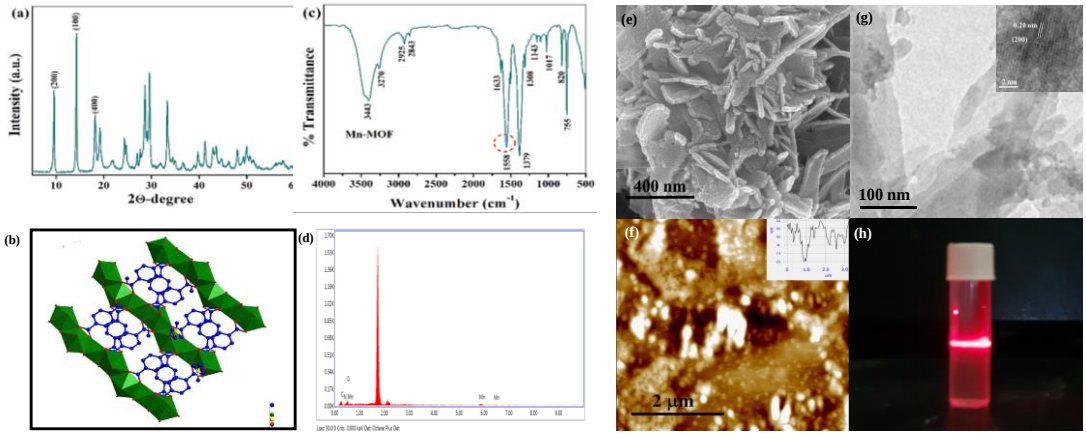

Figure 4.1. (a) Powder XRD pattern of ultrathin Mn-MOF (U) nanosheets; (b) crystal structure of the synthesized Mn-MOF (U) nanosheets; color code: blue-carbon, green-manganese, yellow-nitrogen, red-oxygen; (c) IR spectrum of Mn-MOF (U). The peaks at 1633 cm^{-1} and 1558 cm^{-1} were assigned for C=O bonding of carboxylate group, and peaks at 1379 cm^{-1} and 1308 cm^{-1} were generated from the aromatic carbon C-C double bond stretching vibrations; (d) EDS spectra of Mn-MOF (U) (e) SEM image of Mn-MOF (U) showing the ultrathin nanosheet morphology; (f) AFM topography image of Mn-MOF (U) revealing the thickness of the ultrathin nanosheets to be ~9 nm (inset: height profile) (g) TEM image of Mn-MOF (U) confirming the ultrathin morphology of the nanosheets (inset: HRTEM showing the lattice spacing of 0.20 nm indexed for the (200) plane of Mn-MOF (U), and (h) Tyndall effect evidencing the presence of ultrathin nanosheets.

Fourier transformed infrared (FT-IR) spectrum of Mn-MOF (U) showed the characteristic peak of bridging carboxylic acid group at 1558 cm^{-1} lower than that of free BDC (1690 cm^{-1}, Figure 4.1c).[31] Energy-dispersive X-ray spectroscopic (EDX) studies confirmed the presence of the elements Mn, C, N, and O, (Figure 4.1d) whereas Mn-MOF (B) showed the presence of Mn, C, and O (Figure 4.2c). The morphology of Mn-MOF (U) was investigated by field emission scanning electron microscopic (FE-SEM) and transmission electron microscopic (TEM) studies. FE-SEM image of Mn-MOF (U) showed 2D ultrathin nanosheets. The thickness of the upstanding nanosheets was determined to be 8-12 nm (Figure 4.1e). SEM studies of Mn-MOF (B) showed 3D irregular morphology with agglomerated structure (Figure 4.2b). TEM image revealed transparent and atomic level thick nanosheets of ultrathin Mn-MOF (U) (Figure 4.1g). HR-TEM exhibited the lattice spacing of 0.20 nm corresponding to the (200) plane of Mn-BDC (Figure 4.1g, inset).[32] TEM images of Mn-MOF (B) detected the particles with irregular shape (Figure 4.2d). Atomic force microscopic (AFM) image showed the thickness of the Mn-MOF (U) nanosheets to be ~9 nm (Figure 4.1f). The atomic-level thickness of Mn-MOF (U) was also confirmed by the Tyndall effect. Scattering of the light was observed when the dispersion of Mn-MOF (U) in ethanol was irradiated with a Laserbeam (Figure 4.1h).

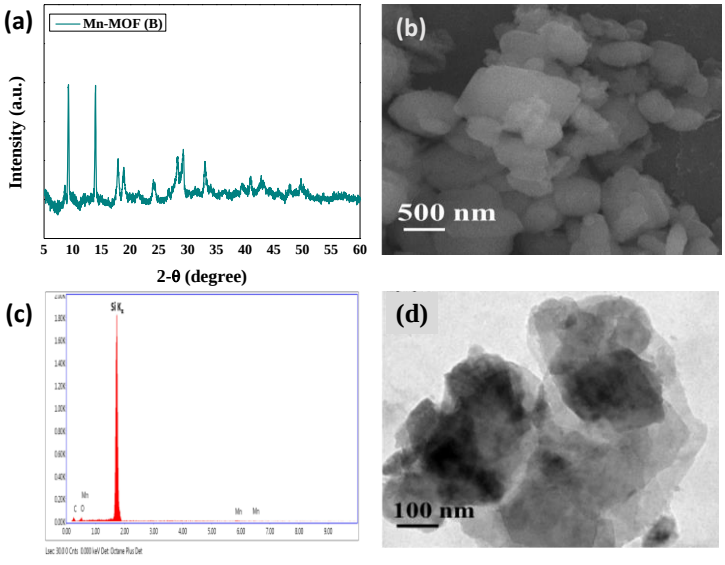

Figure 4.2. (a) Powder XRD pattern of bulk Mn-MOF (B) (b) SEM image of Mn-MOF (B) (c) EDX spectra (d) TEM image of Mn-MOF (B)

The oxidation states and the electronic environments of the elements in Mn-MOF (U) were investigated by the X-ray photoelectron spectroscopic (XPS) studies. Mn 2p XP spectrum was deconvoluted into two peaks at binding energies 643.15 eV and 653.04 eV corresponding to $2p_{3/2}$ and $2p_{1/2}$, respectively (Figure 4.3a). The peak at 643.15 eV was assigned for Mn^{3+}, whereas the peak at 640.13 eV originated from Mn^{2+}.[33,34] The presence of mixed valent $Mn^{2+/3+}$ was also confirmed by a spin-orbit spacing value of 10.4 eV (Figure 4.3a).[35] O 1s XPS was fitted into two peaks at 530.66 eV attributed to the metal-oxygen bond, and the peak at 531.84 eV was assigned for absorbed water molecules (Figure 4.3b).[33-36] C 1s XP spectrum showed three peaks at binding energies 285.57 eV, 284.79 eV and 283.87 eV (Figure 4.3c). The peak at 285.57 eV was attributed to the C-O bond, and the peak at 284.79 eV was assigned for the C-C bond.[37] The peaks at 283.87 eV corresponded to the M-O-C bond in ultrathin Mn-MOF (U).[38]

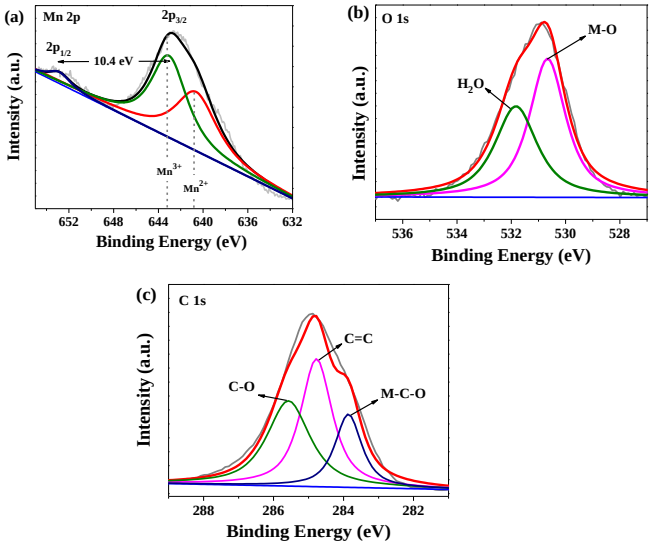

Figure 4.3. (a) Mn 2p XP spectrum of Mn-MOF (U) showed the presence of mixed valent $Mn^{2+/3+}$ (b) O 1s XP spectrum, (c) C 1s XP spectrum

The Mn 2p XPS of the Mn-MOF (B) was deconvoluted into two peaks at binding energies 642.5 eV and 653.6 eV corresponding to $2p_{3/2}$ and $2p_{1/2}$, respectively (Figure 4.4a). The peak at 641.1 eV originated from Mn^{2+}, whereas the peak at 642.5 eV was assigned for Mn^{3+}. The satellite peak corresponding to Mn^{2+} was detected at the binding energy 646.1 eV. O 1s spectrum showed two peaks at binding energies 530.5 and 531.5 eV attributed to the metal-oxygen bond and absorbed water molecules, respectively (Figure 4.4b).[39–41] The XP spectrum of C 1s showed four peaks at binding energies 284.1, 284.6, 285.6, and 288.3 eV corresponding M-O-C bond, C-C bond, C-O bond, and O-C=O bond, respectively (Figure 4.4c).[42]

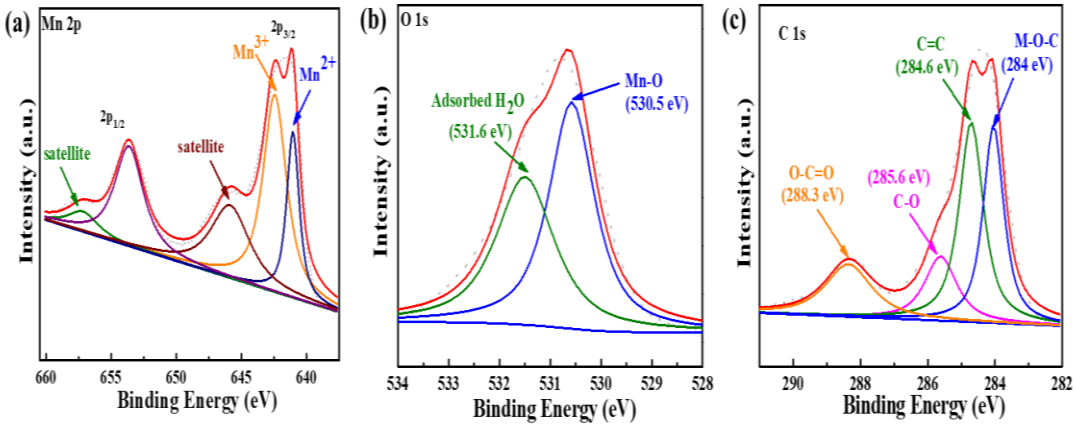

Figure 4.4. (a) Mn 2p XP spectrum of Mn-MOF (B) showed the presence of mixed valent $Mn^{2+/3+}$ (b) O 1s XP spectrum, (c) C 1s XP spectrum.

4.3.2. Evaluation of tribological properties of Mn-MOF (U) and Mn-MOF (B)

4.3.2.1. Dispersion stability

Apart from tribological activity, the stability of the dispersion of the additives is necessarily desired. The determination of dispersion stability of the Mn-MOF (U) and Mn-MOF (B) in paraffin oil (PO) has been accomplished by recording absorbance of the blends (UV/Visible spectroscopy) in the range 200-800 nm from day 0 to day 7 (Figure 4.5). The blends of the optimized concentration (0.15% w/v) in PO were 10 times diluted, and their initial absorbance values were noted. The absorbance data were collected for 7 days. Figure 4.5a delineates the change of relative absorbance against settling time for the synthesized additives. In general, the relative absorbance goes down with time, but the amount of reduction is much lesser in Mn-MOF (U) than Mn-MOF (B) within 7 days. Accordingly, the Mn-MOF (U) shows much higher dispersion stability than Mn-MOF (B). The absorbance pattern of Mn-MOF (U) has been shown in the inset of Figure 4.5a.

Additive absorbs at almost 282 nm. Photographs of dispersion of Mn-MOF (B) and Mn-MOF (U) in the beginning and after 7 days are displayed in Figure 4.5b.

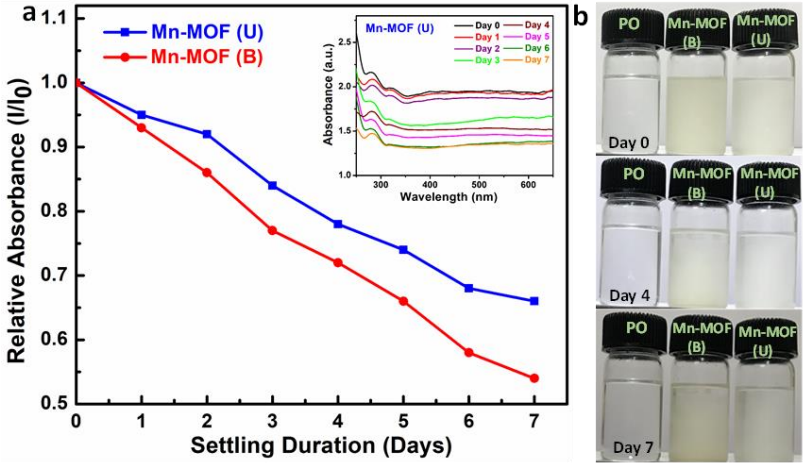

Figure 4.5. (a) Dispersion stability of base oil containing Mn-MOF (B) and Mn-MOF (U) studied by UV-vis spectrophotometry; (b) optical photographs of Mn-MOF (U) and Mn-MOF (B) dispersed in base oil at different settling time (days).

4.3.2.2. Evaluation of Optimized concentration of the additives

The tribological properties, indeed, are dependent on the concentration of the additive. Therefore, admixtures of the additives at varying concentrations 0.00, 0.10, 0.15, and 0.20% w/v in PO were prepared and tested according to antiwear test ASTM D4172 conditions; 392 N applied load run for 60 min at 1200 RPM. The observed mean wear scar diameters (MWD) at various concentrations are illustrated in Figure 4.6a.

For the surface lubricated with plain paraffin oil, the MWD was observed as 0.735 mm, which is remarkably reduced in the presence of blends. At 0.10% concentration of additives, it goes down to 0.540 mm for Mn-MOF (B) whereas 0.535 mm for Mn-MOF (U). The reduction in MWD continues further to 0.520 mm and 0.480 mm for the next

tested concentration, 0.15% w/v of these additives. After that, at 0.20% w/v, there is an increase in MWD to 0.545 mm and 0.520 mm, respectively, for them. Thus, the performance of MOF (U) has always been more significant than MOF (B) at all the tested concentrations. The smallest MWD is obtained at 0.15% w/v concentration for both the additives. Thus, 0.15% of w/v could be identified as the optimized concentration.

4.3.2.3. Antiwear and antifriction properties of the additives

Following ASTM D4172 standards, 1200 rpm, 392 N load, and 60 min time, the antiwear tests of base lube and its admixtures with Mn-MOFs were conducted at the optimized concentration 0.15% w/v. The average coefficient of friction (COF) is a significant parameter related to the longevity of machines. The variation of COF with time for base oil and its blends with the additive following ASTM D4172 conditions is depicted in Figure 4.6b. The average COF for plain oil, 0.079, is lowered considerably in the presence of the additives, 0.052 for Mn-MOF (B), and 0.043 for Mn-MOF (U). Unquestionably, the additive Mn-MOF (U) is showing illustrious performance as an antifriction agent. In general, COF is comparatively higher at the initial stages for the blank oil as well as its blends with the additives. The high COF may be attributed to the absence of the tribofilm in the beginning. With an increase in running time, the tribofilm is formed, and the COF becomes steady. It is a noticeable feature of the graph that COF is quite smooth in the presence of the additive; however, in its absence, the COF is not smooth at all. The smoothness of the plot is directly related to the nature of tribofilm. Thus, it may be inferred that tribofilm formed in the presence of Mn-MOF (U) is quite uniform, strong, adherent, and persistent. Figure 4.6c illustrates the two major tribological parameters,

mean wear scar diameter (MWD) and the average coefficient of friction (COF) concurrently in the form of a bar diagram. The MWD of the base oil, 0.735 mm, has declined to 0.520 mm and 0.480 mm for the blends Mn-MOF (B) and Mn-MOF (U), respectively. The ultrathin nanosheets of Mn-MOF have shown much better performance than the other similar materials reported from our laboratory. For the lamellar structure of reduced graphene oxide (rGO),[24,42] and molybdenum disulphide (MoS_2)[26,42] the reduction in MWD was observed around 11% and 15%, respectively under similar conditions, whereas in the case of Mn-MOF (B) and MOF (U) it reaches to 29, and 35% respectively.

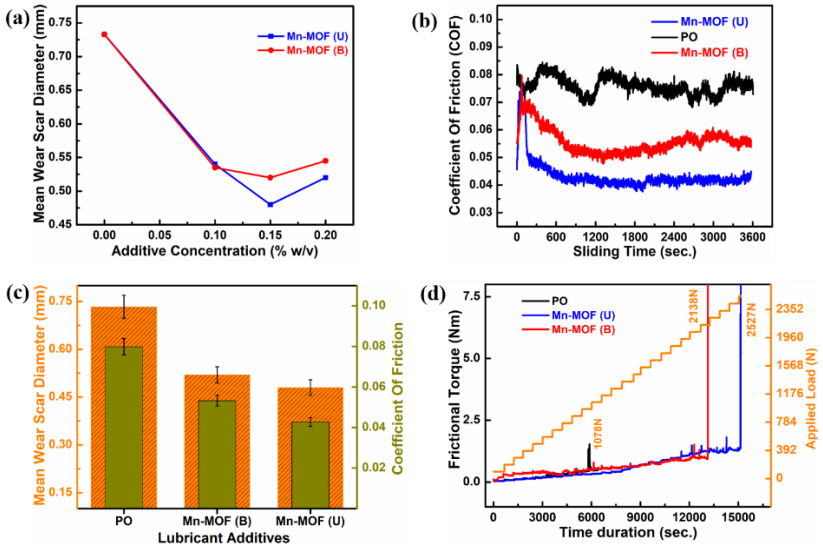

Figure 4.6. (a) Variation of mean wear scar diameter for the paraffin oil as a function of additive concentration at 392 N applied load for 60 min duration (b) coefficient of friction as a function of sliding time (c) Bar diagram for mean wear scar diameter and the average coefficient of friction (d) Variation of frictional torque as a function of stepwise loading and time for PO in the absence and presence of additives

4.3.2.4. Load bearing test

The ASTM D5183 test conditions were followed to perform the load-bearing test. The test was first conducted to complete the running-in period under the test conditions; 392 N load, 600 RPM, 75 °C temperature, 60 min. It was further resumed with consecutive inclusion of 98 N load after 10 min interval till the attainment of seizure load. Figure 4.6d narrates the variation of frictional torque with time and load simultaneously for paraffin oil and its blends with the additives. It is evident from Figure 4.6d that the paraffin oil fails to bear the load at 1078 N. On the other hand, the seizure load is observed at 2138 N for Mn-MOF (B) while 2527 N for Mn-MOF (U). Thus, there is sufficient enhancement in the load-carrying capacity of the oil in the presence of the ultrathin MOF.

4.3.2.5. Frictional power loss

The frictional power loss (P) was calculated for paraffin oil with and without Mn-MOF additives using the given equation (4.1).

$$P = 221 \times \mu (W) \quad (4.1)$$

Where, μ = coefficient of friction

$$1kWh = 3.6MJ \quad (4.2)$$

The highest power consumption (0.062 MJ) was observed for plain paraffin oil. In the presence of the additives, its value decreases to 0.0421 MJ for Mn-MOF (B) and 0.0339 MJ Mn-MOF (U). As evident from the data, more energy is saved in the case of MOF (U) compared to MOF (B).

Table 4.1. Loss of frictional power measured for different additives at the concentration, 0.15% (w/v) in PO

S.N.	Additives	Power consumption (MJ)	Reduction in Power consumption	% Reduction in Power consumption
1.	PO	0.062	____	____
2.	Mn-MOF (B)	0.0421	0.0199	32.2
3.	Mn-MOF (U)	0.0339	0.0281	45.6

4.3.3. Morphological studies of the worn surface

The steel balls after ASTM D4172 test were washed with n-hexane, dried, and then morphology of the wear track in the presence of base oil with or without additive was inspected using surface techniques, SEM and AFM. The SEM images presented in Figure 4.7 show furrows when the surface is lubricated with oil alone; however, it is highly smoothened in the presence of the blends. The values of MWD are shown in the inset of the images. Thus, for the surface lubricated with blends, almost 29% reduction in the MWD is perceptible in the case of Mn-MOF (B) and nearly 35% for Mn-MOF (U). The EDX spectrum of the worn surface in the presence of Mn-MOF (U) is shown in Figure 4.7d. It is discernible that manganese is present on the worn surface along with carbon and oxygen. Thus, manganese is actively involved in tribofilm formation giving fabulous tribo performance. At high pressure applied during tribological activity measurement, the 3D structure of bulk Mn-MOF is disturbed and converted into nanosheets. It is a common

technique of forming ultrathin materials from the bulk.[43,44] In the presence of the 3.4 GPa pressure during tribological activity testing, the monolayers from the bulk 3D MOF come out to form 2D nanosheets. As a result, a significant difference was not observed from the SEM studies of the worn surfaces lubricated by Mn-MOF (B) and Mn-MOF (U).

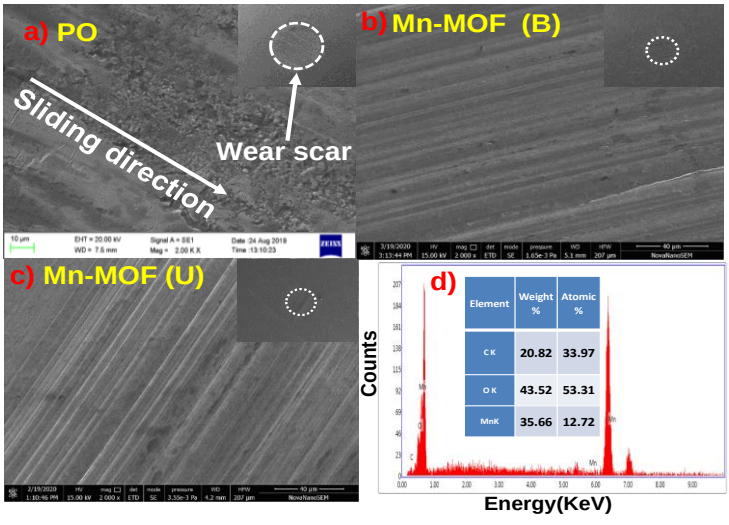

Figure 4.7. (a), (b), and (c) SEM micrographs (inset: full view of wear scar at 100X, wear scar surface at 2.00 KX magnification) of the worn steel surface lubricated with paraffin oil without and with additives (0.15% w/v) (d) EDX spectra of the worn surface lubricated with PO blended with 0.15% w/v Mn-MOF (U) after ASTM D4172 test

The surface of the wear scar has been investigated by AFM studies as well. AFM micrographs of the wear scar were recorded for oil with and without additive after performing the antiwear test. Figure 4.8 narrates the 3D images of the worn surfaces together with area and line roughness data Sq and Rq, respectively. The Sq value for blank oil 626 nm has reduced to 312 nm and 171 nm for oil blended with Mn-MOF (B) and Mn-MOF (U), respectively. Similarly, the Rq value also has shown a reduction from

plain oil (919 nm), Mn-MOF (B) (362 nm), and Mn-MOF (U) (151 nm). The observed roughness data also validate the tribological data.

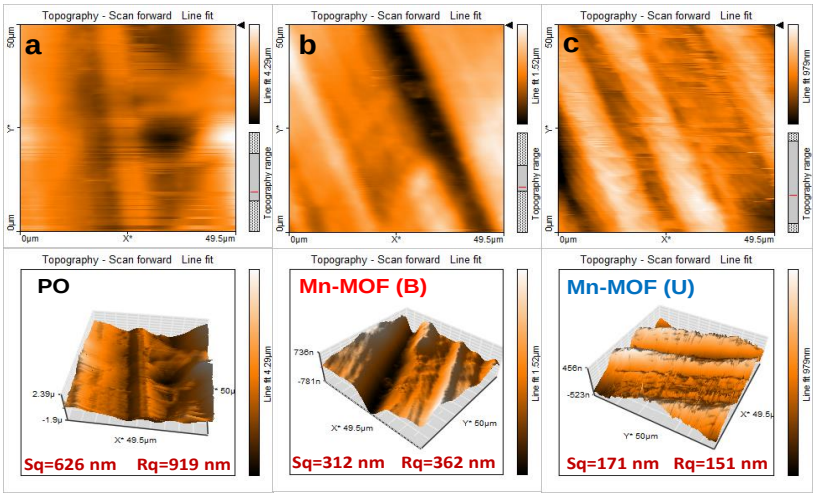

Figure 4.8. 2D and 3D AFM images of the worn steel surface lubricated with blank paraffin oil (PO) and blends of PO with 0.15% w/v of the additives at 392 N applied load

The electronic environment and oxidation states of the elements on the worn surface were determined by XPS studies (Figure 4.9). High-resolution Mn 2p spectrum was deconvoluted into three peaks corresponding to Mn^{2+}, $Mn^{3+,}$ and Mn^{4+} species (Figure 4.9a).[45–47] This result indicates the oxidation of Mn^{2+} in Mn-MOF (U) to a higher oxidation state with applied high pressure during testing. Fe 2p XP spectrum showed the feature of Fe_2O_3 (Figure 4.9b).[24-26,48] Important information about the structural changes of Mn-MOF (U) during testing was derived from the O 1s spectrum (Figure 4.9c). The O 1s peak was deconvoluted into three peaks. The new peaks at 529.2 eV and 530.3 eV were originated from the Mn-O-Mn and Mn-OH species, which clearly showed the transformation of the ultrathin MOF into a mixed valent manganese oxide (Mn^{2+}, Mn^{3+},

and Mn^{4+}) structure.[33-36] The peak at 531.3 eV was assigned for the surface adsorbed water molecule. The C 1s spectrum (Figure 4.9d) can be fitted into two peaks corresponding to C=C and C-O species.[37]

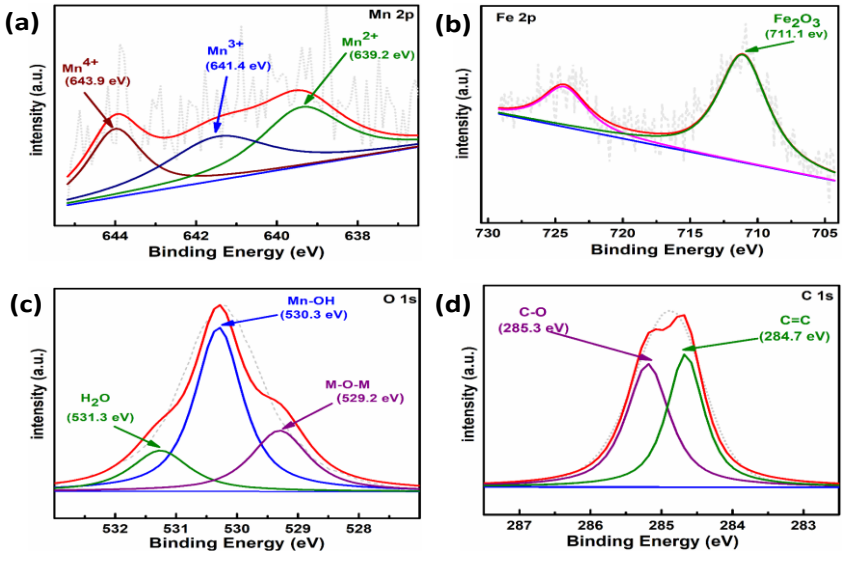

Figure 4.9. XP spectra of the tribofilm formed on the steel surface lubricated with Mn-MOF (U) under ASTM D4172 test conditions: (a) Mn 2p spectra, (b) Fe 2p spectra, (c) O 1s spectra, and (d) C 1s spectra

4.4. Conclusions

Ultrathin manganese-based 2D-metal organic framework nanosheets were synthesized by seizing the 3D growth in the presence of a strong sigma donating ligand. The thickness of the Mn-MOF (U) was determined to be 9 nm. The newly synthesized 2D-ultrathin MOF was found to show illustrious tribological performance in paraffin oil as manifested from its tribological data, namely MWD, COF, seizure load, and frictional power loss. EDX and XPS studies of the tribofilm on the wear track of steel ball supported the observed results. SEM and AFM studies of the worn surface exhibited highly improved

smoothening than paraffin oil alone. The tribological activity of Mn-MOF (U) showed apparent enhancement as compared to that of Mn-MOF (B). It could be correlated with the facilitated ease of sliding nanosheets in the former and restrained in the latter. Thus, the antiwear and friction-reducing mechanism of Mn-MOF (U) can be explained on the basis of the presence of weak van der Waals forces between the adjacent nanosheets in 2D materials, which promote their shearing under sliding motion.

4.5. References

(1) Dutta, S.; Liu, Z.; Han, H.; Indra, A.; Song, T. Electrochemical Energy Conversion and Storage with Zeolitic Imidazolate Framework Derived Materials: A Perspective. *ChemElectroChem* **2018**, *5* (23), 3571–3588.

(2) Singh, B.; Indra, A. Designing Self-Supported Metal-Organic Framework Derived Catalysts for Electrochemical Water Splitting. *Chem. – Asian J.* **2020**, *15* (6), 607–623.

(3) Indra, A.; Song, T.; Paik, U. Metal Organic Framework Derived Materials: Progress and Prospects for the Energy Conversion and Storage. *Adv. Mater.* **2018**, *30* (39), 1705146.

(4) Zhao, Y.; Song, Z.; Li, X.; Sun, Q.; Cheng, N.; Lawes, S.; Sun, X. Metal Organic Frameworks for Energy Storage and Conversion. *Energy Storage Mater.* **2016**, *2*, 35–62.

(5) Wu, H. B.; Lou, X. W. (David). Metal-Organic Frameworks and Their Derived Materials for Electrochemical Energy Storage and Conversion: Promises and Challenges. *Sci. Adv.* **2017**, *3* (12), eaap9252.

(6) Peng, Y.; Li, Y.; Ban, Y.; Yang, W. Two-Dimensional Metal–Organic Framework Nanosheets for Membrane-Based Gas Separation. *Angew. Chem.* **2017**, *129* (33), 9889–9893.

(7) Xiao, X.; Zou, L.; Pang, H.; Xu, Q. Synthesis of Micro/Nanoscaled Metal–Organic Frameworks and Their Direct Electrochemical Applications. *Chem. Soc. Rev.* **2020**, *49* (1), 301–331.

(8) Li, X.; Yang, X.; Xue, H.; Pang, H.; Xu, Q. Metal–Organic Frameworks as a Platform for Clean Energy Applications. *EnergyChem* **2020**, *2* (2), 100027.

(9) Khandelwal, G.; Maria Joseph Raj, N. P.; Kim, S.-J. Zeolitic Imidazole Framework: Metal–Organic Framework Subfamily Members for Triboelectric Nanogenerators. *Adv. Funct. Mater.* **2020**, *30* (12), 1910162.

(10) Shi, Q.; Chen, Z.; Song, Z.; Li, J.; Dong, J. Synthesis of ZIF-8 and ZIF-67 by Steam-Assisted Conversion and an Investigation of Their Tribological Behaviors. *Angew. Chem.* **2011**, *123* (3), 698–701.

(11) Wang, F.-F.; Liu, Z.; Cheng, Z.-L. High Performance of MOF-Structured Lubricating Material with Nano- and Micro-Sized Morphologies. *Mater. Lett.* **2019**, *248*, 222–226.

(12) Zhang, G.; Xie, G.; Si, L.; Wen, S.; Guo, D. Ultralow Friction Self-Lubricating Nanocomposites with Mesoporous Metal–Organic Frameworks as Smart Nanocontainers for Lubricants. *ACS Appl. Mater. Interfaces* **2017**, *9* (43), 38146–38152.

(13) Zhang, S.; Ma, T.; Erdemir, A.; Li, Q. Tribology of Two-Dimensional Materials: From Mechanisms to Modulating Strategies. *Mater. Today* **2019**, *26*, 67–86.

(14) Berman, D.; Erdemir, A.; Sumant, A. V. Approaches for Achieving Superlubricity in Two-Dimensional Materials. *ACS Nano* **2018**, *12* (3), 2122–2137.

(15) Wang, F.-F.; Fan, L.; Liu, Z.; Cheng, Z.-L. Surfactant-Mediated Preparation and Tribological Behaviors of Few-Layer ZnBDC. *Mater. Lett.* **2019**, *257*, 126757.

(16) Jaiswal, V.; Kalyani; Rastogi, R. B.; Kumar, R. Tribological Studies of Some SAPS-Free Schiff Bases Derived from 4-Aminoantipyrine and Aromatic Aldehydes and Their Synergistic Interaction with Borate Ester. *J. Mater. Chem. A* **2014**, *2* (27), 10424–10434.

(17) Jaiswal, V.; Gupta, S. R.; Rastogi, R. B.; Kumar, R.; Singh, V. P. Evaluation of Antiwear Activity of Substituted Benzoylhydrazones and Their Copper(II) Complexes in Paraffin Oil as Efficient Low SAPS Additives and Their Interactions with the Metal Surface Using Density Functional Theory. *J. Mater. Chem. A* **2015**, *3* (9), 5092–5109.

(18) Kavita; Verma, P.; Verma, D. K.; Kumar, B.; Singh, A. K.; Shukla, N.; Srivastava, V.; Rastogi, R. B. Tetrahydropyrazolopyridines as Antifriction and Antiwear Agents: Experimental and DFT Calculations. *RSC Adv.* **2020**, *10* (17), 10188–10196.

(19) Jaiswal, V.; Rastogi, R. B.; Kumar, R.; Singh, L.; Mandal, K. D. Tribological Studies of Stearic Acid-Modified $CaCu_{2.9}Zn_{0.1}Ti_4O_{12}$ Nanoparticles as Effective Zero SAPS Antiwear Lubricant Additives in Paraffin Oil. *J. Mater. Chem. A* **2014**, *2* (2), 375–386.

(20) Kalyani; Rastogi, R. B.; Kumar, D. Synthesis, Characterization, and Tribological Evaluation of SDS-Stabilized Magnesium-Doped Zinc Oxide ($Zn_{0.88}Mg_{0.12}O$) Nanoparticles as Efficient Antiwear Lubricant Additives. *ACS Sustain. Chem. Eng.* **2016**, *4* (6), 3420–3428.

(21) Kumar, B.; Verma, D. K.; Singh, A. K.; Kavita; Shukla, N.; Rastogi, R. B. Nanohybrid Cu@C: Synthesis, Characterization and Application in Enhancement of Lubricity. *Compos. Interfaces* **2020**, *27* (8), 777–794.

(22) Kumar, B.; Verma, D. K.; Shukla, N.; Singh, A. K.; Kavita; Rastogi, R. B. Ionic Liquid Stabilized Ag@C Composite for Improvement of Triboactivity. *J. Mol. Liq.* **2020**, *307*, 113012.

(23) Jaiswal, V.; Kalyani; Umrao, S.; Rastogi, R. B.; Kumar, R.; Srivastava, A. Synthesis, Characterization, and Tribological Evaluation of TiO_2-Reinforced Boron and Nitrogen Co-Doped Reduced Graphene Oxide Based Hybrid Nanomaterials as Efficient Antiwear Lubricant Additives. *ACS Appl. Mater. Interfaces* **2016**, *8* (18), 11698–11710.

(24) Verma, D. K.; Kumar, B.; Kavita; Rastogi, R. B. Zinc Oxide- and Magnesium-Doped Zinc Oxide-Decorated Nanocomposites of Reduced Graphene Oxide as Friction and Wear Modifiers. *ACS Appl. Mater. Interfaces* **2019**, *11* (2), 2418–2430.

(25) Verma, D. K.; Kuntail, J.; Kumar, B.; Singh, A. K.; Shukla, N.; Kavita; Sinha, I.; Rastogi, R. B. Amino Borate-Functionalized Reduced Graphene Oxide Further Functionalized with Copper Phthalocyanine Nanotubes for Reducing Friction and Wear. *ACS Appl. Nano Mater.* **2020**, *3* (6), 5530–5541.

(26) Verma, D. K.; Shukla, N.; Kumar, B.; Singh, A. K.; Shahu, K.; Yadav, M.; Rhee, K. Y.; Rastogi, R. B. Synergistic Tribo-Activity of Nanohybrids of

Zirconia/Cerium-Doped Zirconia Nanoparticles with Nano Lamellar Reduced Graphene Oxide and Molybdenum Disulfide. *Nanomaterials* **2020**, *10* (4), 707.

(27) Zhang, C.; Wu, B.-H.; Ma, M.-Q.; Wang, Z.; Xu, Z.-K. Ultrathin Metal/Covalent–Organic Framework Membranes towards Ultimate Separation. *Chem. Soc. Rev.* **2019**, *48* (14), 3811–3841.

(28) Yin, H.; Tang, Z. Ultrathin Two-Dimensional Layered Metal Hydroxides: An Emerging Platform for Advanced Catalysis, Energy Conversion and Storage. *Chem. Soc. Rev.* **2016**, *45* (18), 4873–4891.

(29) Cai, Z.; Bu, X.; Wang, P.; Ho, J. C.; Yang, J.; Wang, X. Recent Advances in Layered Double Hydroxide Electrocatalysts for the Oxygen Evolution Reaction. *J. Mater. Chem. A* **2019**, *7* (10), 5069–5089.

(30) Zhao, K.; Xu, Z.; He, Z.; Ye, G.; Gan, Q.; Zhou, Z.; Liu, S. Vertically Aligned MnO_2 Nanosheets Coupled with Carbon Nanosheets Derived from Mn-MOF Nanosheets for Supercapacitor Electrodes. *J. Mater. Sci.* **2018**, *53* (18), 13111–13125.

(31) Hu, H.; Lou, X.; Li, C.; Hu, X.; Li, T.; Chen, Q.; Shen, M.; Hu, B. A Thermally Activated Manganese 1,4-Benzenedicarboxylate Metal Organic Framework with High Anodic Capability for Li-Ion Batteries. *New J. Chem.* **2016**, *40* (11), 9746–9752.

(32) Zhao, S.; Wang, Y.; Dong, J.; He, C.-T.; Yin, H.; An, P.; Zhao, K.; Zhang, X.; Gao, C.; Zhang, L. Ultrathin Metal–Organic Framework Nanosheets for Electrocatalytic Oxygen Evolution. *Nat. Energy* **2016**, *1* (12), 1–10.

(33) Indra, A.; Menezes, P. W.; Das, C.; Schmeißer, D.; Driess, M. Alkaline Electrochemical Water Oxidation with Multi-Shelled Cobalt Manganese Oxide Hollow Spheres. *Chem. Commun.* **2017**, *53* (62), 8641–8644.

(34) Menezes, P. W.; Indra, A.; Littlewood, P.; Göbel, C.; Schomäcker, R.; Driess, M. A Single-Source Precursor Approach to Self-Supported Nickel–Manganese-Based Catalysts with Improved Stability for Effective Low-Temperature Dry Reforming of Methane. *ChemPlusChem* **2016**, *81* (4), 370–377.

(35) Menezes, P. W.; Indra, A.; Gutkin, V.; Driess, M. Boosting Electrochemical Water Oxidation through Replacement of Oh Co Sites in Cobalt Oxide Spinel with Manganese. *Chem. Commun.* **2017**, *53* (57), 8018–8021.

(36) Indra, A.; Paik, U.; Song, T. Boosting Electrochemical Water Oxidation with Metal Hydroxide Carbonate Templated Prussian Blue Analogues. *Angew. Chem. Int. Ed.* **2018**, *57* (5), 1241–1245.

(37) Luo, M.; Dou, Y.; Kang, H.; Ma, Y.; Ding, X.; Liang, B.; Ma, B.; Li, L. A Novel Interlocked Prussian Blue/Reduced Graphene Oxide Nanocomposites as High-Performance Supercapacitor Electrodes. *J. Solid State Electrochem.* **2015**, *19* (6), 1621–1631.

(38) Indra, A.; Menezes, P. W.; Kailasam, K.; Hollmann, D.; Schröder, M.; Thomas, A.; Brückner, A.; Driess, M. Nickel as a Co-Catalyst for Photocatalytic Hydrogen Evolution on Graphitic-Carbon Nitride (Sg-CN): What Is the Nature of the Active Species? *Chem. Commun.* **2015**, *52* (1), 104–107.

(39) Indra, A.; Menezes, P. W.; Sahraie, N. R.; Bergmann, A.; Das, C.; Tallarida, M.; Schmeißer, D.; Strasser, P.; Driess, M. Unification of Catalytic Water Oxidation and Oxygen Reduction Reactions: Amorphous Beat Crystalline Cobalt Iron Oxides. *J. Am. Chem. Soc.* **2014**, *136* (50), 17530–17536.

(40) Singh, B.; Prakash, O.; Maiti, P.; Menezes, P. W.; Indra, A. Electrochemical Transformation of Prussian Blue Analogues into Ultrathin Layered Double Hydroxide Nanosheets for Water Splitting. *Chem. Commun.* **2020**, *56* (95), 15036–15039.

(41) Singh, B.; Prakash, O.; Maiti, P.; Indra, A. Electrochemical Transformation of Metal Organic Framework into Ultrathin Metal Hydroxide-(Oxy)Hydroxide Nanosheets for Alkaline Water Oxidation. *ACS Appl. Nano Mater.* **2020**, *3* (7), 6693–6701.

(42) Goel, B.; Vyas, V.; Tripathi, N.; Kumar Singh, A.; Menezes, P. W.; Indra, A.; Jain, S. K. Amidation of Aldehydes with Amines under Mild Conditions Using Metal-Organic Framework Derived NiO@Ni Mott-Schottky Catalyst. *ChemCatChem* **2020**, *12* (22), 5743–5749.

(43) Zhang, K.; Tang, J.; Yuan, J.; Li, J.; Sun, Y.; Matsuba, Y.; Zhu, D.-M.; Qin, L.-C. Production of Few-Layer Graphene via Enhanced High-Pressure Shear Exfoliation in Liquid for Supercapacitor Applications. *ACS Appl. Nano Mater.* **2018**, *1* (6), 2877–2884.

(44) Yi, M.; Shen, Z. A Review on Mechanical Exfoliation for the Scalable Production of Graphene. *J. Mater. Chem. A* **2015**, *3* (22), 11700–11715.

(45) Huang, Z.; Zhou, W.; Ouyang, C.; Wu, J.; Zhang, F.; Huang, J.; Gao, Y.; Chu, J. High Performance of Mn-Co-Ni-O Spinel Nanofilms Sputtered from Acetate Precursors. *Sci. Rep.* **2015**, *5*.

(46) Kim, J.; Heo, J. N.; Do, J. Y.; Chava, R. K.; Kang, M. Electrochemical Synergies of Heterostructured Fe_2O_3-MnO Catalyst for Oxygen Evolution Reaction in Alkaline Water Splitting. *Nanomaterials* **2019**, *9* (10).

(47) Zhang, D.; Zhang, L.; Shi, L.; Fang, C.; Li, H.; Gao, R.; Huang, L.; Zhang, J. In Situ Supported MnO_x–CeO_x on Carbon Nanotubes for the Low-Temperature Selective Catalytic Reduction of NO with NH_3. *Nanoscale* **2013**, *5* (3), 1127–1136.

(48) Shukla, N.; Verma, D. K.; Singh, A. K.; Kumar, B.; Kavita; Rastogi, R. B. Ternary Composite of Methionine-Functionalized Graphene Oxide, Lanthanum-Doped Yttria Nanoparticles, and Molybdenum Disulfide Nanosheets for Thin-Film Lubrication. *ACS Appl. Nano Mater.* **2020**, *3* (8), 8012–8026.